JGR Solid Earth

RESEARCH ARTICLE
10.1029/2018JB016968

Key Points:
- We present a new Upper Carboniferous paleomagnetic pole for South American Plate, with inclination shallowing correction and time control
- The paleosecular variation results indicated that we should avoid the use of recent geomagnetic models as a reference for Kiaman superchron

Supporting Information:
- Supporting Information S1
- Table S1
- Table S2
- Table S3
- Table S4
- Table S5
- Table S6

Correspondence to:
D. Brandt,
daniele.brandt@iag.usp.br

Citation:
Brandt, D., Ernesto, M., Constable, C., Franco, D. R., Carlos Weinschutz, L., de Oliveira Carvalho Rodrigues, P., et al. (2019). New late Pennsylvanian paleomagnetic results from Paraná Basin (southern Brazil): Is the recent Giant Gaussian Process model valid for the Kiaman superchron? *Journal of Geophysical Research: Solid Earth*, *124*, 6223–6242. https://doi.org/10.1029/2018JB016968

Received 1 NOV 2018
Accepted 18 JUN 2019
Accepted article online 24 JUN 2019
Published online 10 JUL 2019

New Late Pennsylvanian Paleomagnetic Results From Paraná Basin (Southern Brazil): Is the Recent Giant Gaussian Process Model Valid for the Kiaman Superchron?

Daniele Brandt[1], Marcia Ernesto[1], Catherine Constable[2], Daniel Ribeiro Franco[3], Luiz Carlos Weinschutz[4], Pillar de Oliveira Carvalho Rodrigues[3], Linda Hinnov[5], Plinio Jaqueto[1], Becky E. Strauss[6,7], Joshua Feinberg[6], Pedro Vitor de Paiva Franco[8], and Xixi Zhao[9]

[1]Instituto de Astronomia, Geofísica e Ciências Atmosféricas, Departamento de Geofísica, Universidade de São Paulo, São Paulo, SP, Brazil, [2]Institute of Geophysics and Planetary Physics, Scripps Institution of Oceanography, University of California at San Diego, La Jolla, CA, USA, [3]Coordenação de Geofísica, Observatório Nacional, Rio de Janeiro, RJ, Brazil, [4]Centro Paleontológico da Universidade do Contestado, Universidade do Contestado, Mafra, Santa Catarina, Brazil, [5]Department of Atmospheric, Oceanic, and Earth Sciences, George Mason University, Fairfax, VA, USA, [6]Institute for Rock Magnetism, Department of Earth Sciences, University of Minnesota, Minneapolis, MN, USA, [7]NIST: National Institute of Standards and Technology, Gaithersburg, MD, USA, [8]Centro de Geociencias, Universidad Nacional Autónoma de México, Querétaro, México, [9]State Key Laboratory of Marine Geology, Tongji University, Shanghai, China

Abstract The most recent Giant Gaussian Process (GGP) model, based on the last 5 Ma, has been used as a reference for directional distribution of paleomagnetic record of older rocks as Cenozoic and Proterozoic. However, for Paleozoic times, its validity has not yet been tested. Here we evaluate the validity of this recent GGP model for the Kiaman superchron. We present new paleomagnetic results from a late Pennsylvanian section of glacial rhythmites (Mafra Formation) from southern Brazil. The 5-m section sampled spans more than 800 kyr, as evaluated by cyclostratigraphic analysis. Thermal demagnetization revealed a reversed characteristic component carried by single domain magnetite. Anisotropy of anhysteretic remanent magnetization indicated a small shallowing correction of $f = 0.97$. The final paleomagnetic pole position is located at 51.9°S, 344.3°E ($N = 111$, $R = 109.0$, $K = 55.9$, $A_{95} = 1.8°$), with a mean direction of Dec = 144.2°, Inc = 69.5° ($N = 111$, $R = 110.2$, $k = 134.4$, $\alpha_{95} = 1.2°$, Paleolat = 53.2°S). The shape of the distribution of magnetization directions (elongation $E = 2.08^{3.13}_{1.44}$) and the dispersion of virtual geomagnetic poles ($S_V = 10.9^{11.8}_{9.8}$) are incompatible with the recent model. The reduced dispersion, also found in other studies, implies a different shape in directional distributions for any GGP model describing the Kiaman interval. This result alerts us that we should abandon the use of the recent GGP model as a reference for inclination shallowing correction of Carboniferous sedimentary data.

1. Introduction

Determination of the past configuration of supercontinents is possible because of the fundamental geocentric axial dipole (GAD) hypothesis of paleomagnetism. According to this hypothesis, the time-averaged geomagnetic field can be described as a magnetic dipole at the center of the Earth aligned to the rotation axis. The mean GAD with small contributions (less than 5%) of persistent nondipolar components is confirmed by paleosecular studies in sediments and lavas from the last 10 million years (Cromwell et al., 2018; Johnson et al., 2008; Opdyke & Henry, 1969).

Statistical paleosecular variation (PSV) models can describe this mean geomagnetic field and its long-term variations. The Giant Gaussian Process (GGP) type are PSV models that are capable of predicting a distribution of directions anywhere on the Earth (Constable & Johnson, 1999; Constable & Parker, 1988; Quidelleur & Courtillot, 1996; Tauxe & Kent, 2004). They are based on the concept that long-timescale variation of the geomagnetic field can be described by statistical fluctuation of the gauss coefficients around mean values (g_l^m and h_l^m) and standard deviations (σ_l) that are a function of their degree, l, and proportional to a fitted parameter α. Each gauss coefficient has a mean value corresponding to the description of the

time-averaged field in terms of spherical harmonic functions, so if the model describes a mean GAD, all the coefficients have a null mean, except for g_1^0.

The most recent GGP model fitted for the recent field (0 to 5 Ma) is the TK03.GAD model (Tauxe & Kent, 2004), which best describes the paleosecular variation recorded by recent lavas database of McElhinny and McFadden (1997). According to TK03.GAD, the distribution of directions should be elongated along the vertical and North-South plane, and this elongation should decay from almost three at the Equator to one (circular) at the poles. The elongation E, as described by Tauxe and Kent (2004), is determined by the ratio between intermediate and minimum eigenvalues (τ_2/τ_3) from the "orientation matrix" T (Scheidegger, 1965). If a group of magnetic remanence directions accurately records the geomagnetic field, it should have a mean and distribution shape compatible with that predicted by the model. Tauxe et al. (2008) and Tauxe and Kodama (2009) tested the TK03.GAD model, proposed by Tauxe and Kent (2004), for rocks older than 5 Ma and found good agreement for paleomagnetic data from Cenozoic and Proterozoic ages.

The TK03.GAD model has been used as a reference for correction of sedimentary data supposedly affected by inclination shallowing. The elongation/inclination (E/I) method (Tauxe & Kent, 2004) was proposed to correct the difference in inclination produced by shallowing. According to this method, if a long section of sedimentary data has been affected by inclination shallowing, its distribution would be deformed, and the elongation that should be in the north-south direction would diminish until it becomes an East-West squeezed elongation. The E/I method finds a flattening factor correction f in which the pair E/I is made compatible with that predicted by TK03.GAD model. The f factor can be described as $f = \tan I_O / \tan I_f$ (King, 1955), where I_f is the real field and I_0 is the flattened observed inclination.

Shallowing correction has become a mandatory procedure for the late Paleozoic rocks, since the majority of data of this age are derived from sedimentary rocks (Torsvik et al., 2012), and because of the absence of inclination shallowing correction, these data have been pointed as the cause of paleolatitudes overlapping error in Pangea reconstruction (Domeier et al., 2012; Irving, 1977). There are two independent ways to do shallowing correction: by the use of anisotropy of anhysteretic remanent magnetization (AARM), first proposed by Jackson et al. (1991), and the E/I method. The former procedure is related to the magnetic fabric of the rocks and does not depend on any model of geomagnetic field. The E/I method depends on the geomagnetic record, and its validity has not been tested for Paleozoic times. Even so, it has been applied by some authors (e.g., Brandt et al., 2009; Franco, Ernesto, et al., 2012; Haldan et al., 2009; Lanci et al., 2013).

The end of the Paleozoic Era is marked by the occurrence of the longest Phanerozoic superchron, which is of reversed polarity and is called the Permo-Carboniferous Reversed superchron or Kiaman. Superchrons are long time intervals (tens of millions of years) when the geomagnetic field stayed in one stable polarity, and its secular variation was more suppressed. Dispersion of virtual geomagnetic poles (VGPs) of superchrons is smaller for low and medium latitudes and has a more prominent increase with latitude than is observed for the last 5-Ma field or other high-frequency reversal times (Biggin et al., 2008; de Oliveira et al., 2018; McFadden et al., 1991). However, Doubrovine et al. (2019) analyzed the paleosecular variation estimates for the CNS and the pre-CNS (198–126 Ma) using an updated volcanic database and, comparing to recent compilations for the last few million years (e.g., Cromwell et al., 2018), concluded that the differences in the latitude behavior of PSV during intervals of stable and high-variability field do not allow the use of this proxy to evaluate the geomagnetic field stability. That conclusion does not mean that the TK03.GAD gives similar VGP dispersion as a superchron because the TK03.GAD model was determined with a database [McElhinny & McFadden, 1997] with larger VGP dispersion and with less variation in latitudes than a superchron. Therefore, it seems natural to us that if the Kiaman's dispersion of VGPs is so different from this model, then the directional distribution should also be different.

Attempts to test the validity of TK03.GAD for Kiaman times were done with two groups of paleomagnetic data from long sections of igneous records (Bazhenov et al., 2016; Haldan et al., 2014). Both results presented distributions with elongation smaller than that predicted by TK03.GAD model, but because of high values of uncertainty on elongation results, the analyses of those results on their own were not conclusive.

The present paper presents new and detailed paleomagnetic results from a Carboniferous sedimentary section from the Mafra Formation (Itararé Group, Paraná Basin, southern Brazil). We applied AARM

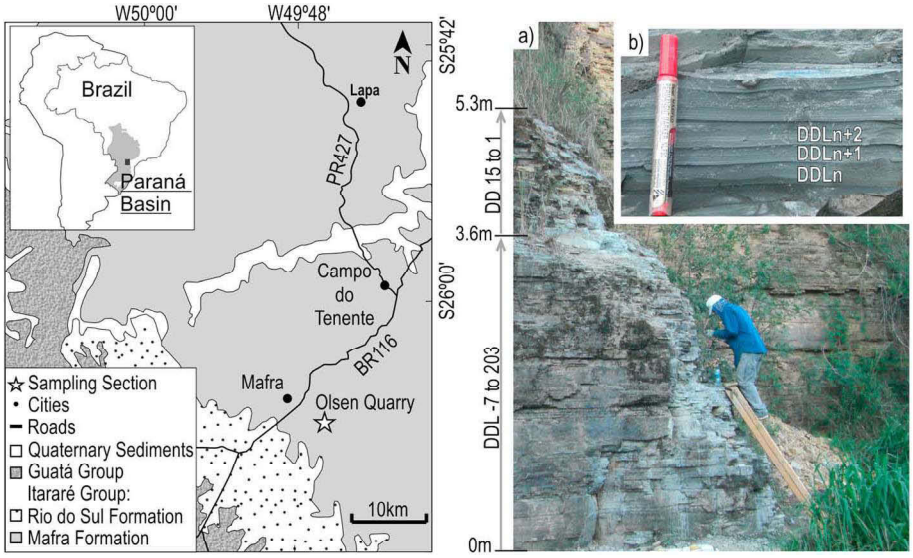

Figure 1. Location of sampling section (Olsen Quarry) at the geological map of the region. Dots are the Cities of Mafra, Campo do Tenente, and Lapa (Santa Catarina State). (a) Sampling section with the stratigraphic localization of DDL layers (samples to paleomagnetic and cyclostratigrafic analyses) and localization of DD layers (samples only for paleomagnetic analyses). (b) Detail of the rhythmites layers and the naming scheme of DDL part.

shallowing correction to the magnetic record and cyclostratigraphic analysis to infer if the elapsed time was sufficient to properly record the paleosecular variation of the geomagnetic field. This new data set is shown to be an accurate record of paleosecular variation, which allowed us to verify the applicability of E/I method for rocks of approximately the same age. We also run simulations of GGP models with lower values of dispersion of VGPs and higher latitudinal variation (as expected for a superchron) in order to find a GGP model that could explain the Mafra dispersion and elongation results.

2. Geological Setting and Sampling

Paraná Basin is an extensive intracratonic basin located in the center-eastern part of the South American plate. It covers the southern region of Brazil and parts of Uruguay, Argentina, and Paraguay. The subsidence and sedimentation of Paraná Basin started during Ordovician times (Milani, 1997). The glacial deposits of the Itararé Group are related to the third glacial cycle, which were the most extensive Gondwana glaciation of Phanerozoic. The best outcrops of this unit are at the eastern and northeastern border of Paraná Basin. Following Schneider et al. (1974), the sedimentation of Itararé Group begins with Campo do Tenente (Medium Carboniferous) and finishes with Rio do Sul formations (Early Permian). The Mafra Formation, whose rhythmites are the target of this work, is positioned between those two formations, and its deposition is attributed to the Late Pennsylvanian (Kasimovian to Gzhelian). This age was determined by palynostratigraphy, where the Late Carboniferous palynozone *Crucisaccites monoletus* were correlated to the middle portion of the Itararé Group (Holz et al., 2008).

The Mafra formation is composed of diamictites, sandstones, rhythmites, and mudstones. The sampled rhythmite section is located in an inactive quarry named Olsen (26.14°S, 310.24°E, star in the geological map of Figure 1), near Mafra City. According to Weinschütz and Castro (2004), it is related to the middle portion of the Mafra Formation and is composed of pairs of light-colored siltites and fine layers of dark clay, with variable thickness of some millimeters up to 5 cm at maximum. These layers repeat all along the whole quarry, reaching a total thickness of a few tens of meters and hundreds of meters of lateral extension. The layers are flat and preserve the paleohorizontal plane.

The paleomagnetic sampling was performed through a 5-m-high wall comprising 216 of distinct layers. A total of 124 oriented blocks were collected and oriented by sun and magnetic compasses. The bottom part was sampled in detail: 201, from existing 211 pairs (layers), were sampled. This bottom part is 3.6 m of height, and its layers were named "DDL." Figure 1a shows the sampling section and stratigraphic

location of DDL layers. Owing to difficulty of access, the top portion was not as comprehensively sampled; only 15 oriented hand samples were distributed along 1.7 m. This top part was named DD and the layers range from DD1 to DD15. The whole section was considered for paleomagnetic analysis. However, only the detailed bottom part (DDL portion) was considered for cyclostratigraphic analyses.

3. Materials and Methods

Laboratory procedures and analysis in this study involved paleomagnetism, rock magnetism, anisotropy of anhysteretic remanence, and cyclostratigraphy.

3.1. Paleomagnetic Procedures

Cylinders of 2.5-cm diameter and up to 2.1 cm high were cut from oriented hand samples in a core drill system in the Paleomagnetic Laboratory of the University of São Paulo (USPmag). Cylinders composed of more than one layer (light/dark pair) were sliced into separate layers. Layers thicker than 2.1 cm were sliced into two specimens. Demagnetization experiments were conducted in a magnetically shielded room with ambient field less than 500 nT. Remanent magnetization measurements were obtained using a superconducting rock magnetometer from 2G Enterprises. Thermal demagnetization was carried out in a thermal specimen demagnetizer from ASC (model TD48) with 9 to 35 heating steps from room temperature to 700 °C. Bulk susceptibility was monitored during the thermal treatment using a Bartington MS2B. Detailed alternating field (AF) demagnetizations with 20 to 30 steps reached peak fields up to 160 mT and were automatically performed in a set of coils coupled to a 2G magnetometer using random sequences of demagnetization axes to avoid systematic contribution of gyroremanent magnetization.

Principal component (Kirschvink, 1980) and great circle (Halls, 1976) analyses were conducted using the Remasoft software (Chadima & Hrouda, 2006). Grouping of magnetic directions in each layer (stratigraphic level) was evaluated by the Fisher's (1953) statistics, and the combination of directions and planes followed the method of McFadden and McElhinny (1988) with specification of constraint arcs.

Inclination shallowing correction was performed using anisotropy of AARM measurements, following Jackson et al. (1991). The procedure of AARM acquisition was done using six different axes in the set of coils that are coupled to the 2G magnetometer, and tensorial analyses of AARM data were done using the Anisoft data browser 5 (Chadima & Jelínek, 2008).

Calculation of VGPs, application of variable cutoff colatitude angles (Vandamme, 1994), calculation of dispersion of VGPs (S), and elongation of the distribution of directions (E) with bootstrap confidence limits followed the procedures described in Tauxe, Banerjee, et al. (2016). Simulations of GGP models were done using a modified mktk03 function from the PMAGPY package of Tauxe, Shaar, et al. (2016).

3.2. Rock Magnetism

Irregular first-order reversal curves (FORCs) were obtained at room temperature using a Princeton Vibrating Sample Magnetometer MicromagTM 3900. The measurement script, processing, and analyses were done using the xFORC software (Zhao et al., 2015). The diagnosis of magnetic domain structure using FORC diagrams followed the procedures of Hu et al. (2018) and Zhao et al. (2017).

Low-temperature magnetization curves of magnetic extracts were obtained at the Institute of Rock Magnetism with a Magnetic Property Measurement System by Quantum Design. Six samples distributed along the studied section were subjected to low-temperature rock magnetism experiments. The magnetic extraction of rock samples was made following Strauss et al. (2013) and Strehlau et al. (2014). Room temperature remanence measurements were made during thermal cycling, where the samples were first subjected to a saturation isothermal remanent magnetization at room temperature and then measured at every 5 K during cooling and heating. Field cooled (FC) and zero-field cooled (ZFC) experiments were also conducted. In these experiments, measurements were taken during heating from 1 K to room temperature. These two experiments differ in the way that the sample is magnetized. In the FC experiment, the sample is first cooled from room temperature to 10 K in the presence of a saturation field; then, the magnetic remanence is measured in steps of 5 K during the warming process. The ZFC experiment consists of cooling a sample in the absence of any magnetic field, inducing a saturation field in low temperatures, and then measuring the remanent magnetization during the warming process.

3.3. Cyclostratigraphic Analysis

As discussed by some authors (e.g., Ellwood et al., 2000, 2012; Fang et al., 2017; Franco, Hinnov, & Ernesto, 2012; Wu et al., 2012), variations in magnetic susceptibility (χ) due to changes in the detrital content of sediments have been widely used in cyclostratigraphic works because they can indicate climatically or eustatically controlled weathering inputs. However, the determination of the origin of χ variations can be tricky because several factors (e.g., grain size and shape, composition, and concentration) can alter χ values (Ellwood et al., 2000). Anhysteretic remanent magnetization (ARM) has been increasingly employed as an alternative method in cyclostratigraphic investigations (e.g., Fang et al., 2017; Kodama et al., 2010; Lanci et al., 2010), as it measures the low-coercivity, fine-grained (<20 μm) ferromagnetic minerals (sensu stricto), for which is often easier to determine the provenance (Latta et al., 2006; Wu et al., 2012). For a better assessment and comparisons of the embedded quasiperiodic harmonic content, both χ and ARM data sets were considered in this study. This approach can also provide better estimates for the depositional time range related to these rocks.

χ and ARM data were determined along the entire DDL section for every sedimentary layer (201 layers). Susceptibility measurements were conducted using an MFK1-FA Kappabridge (AGICO), and ARM acquisition and measurements were done using the 2G magnetometer. The χ and ARM data sets were linearly interpolated and resampled every 1.75 and 1.80 cm, the median spacings of the two series, respectively, and pre-whitened prior to spectral analysis by estimating and removing smoothed curve using MATLAB's *smooth.m* with the "loess" option and a running window that is 60% of the data length (Figures 7a and 7b). Spectral analysis was carried out with the prolate multitaper spectral estimator (Thomson, 1982), with hypothesis testing using a classical order 1 autoregressive red-noise null model (e.g., Mudelsee, 2014) using the MATLAB script *classicredpad.m*. The persistence and/or transience of frequencies along the series was evaluated with evolutionary fast Fourier transform (FFT) analysis using the MATLAB script *evofft.m*. These latter two scripts are available at http://mason.gmu.edu/~lhinnov/cyclostratigraphytools.html. The identification of potential astronomical frequencies was done by comparison of spectral peaks at frequencies that correspond to those of the Earth's orbital eccentricity, obliquity, and precession index predictions for the Upper Carboniferous-Lower Permian interval (298 Ma) by Berger and Loutre (1994).

4. Remanent Magnetization of Mafra Rocks

The thermal demagnetization data revealed the presence of two components in almost all demagnetized specimen, while the AF procedure mostly indicated the presence of more than one component, but did not discriminate the direction very well, and presented noisy behavior at the last few steps of demagnetization (which we eliminated from our directional analyses). A total of 528 specimens were subjected to the demagnetization process. AF demagnetization was applied to all 216 sampled layers (stratigraphic sites), which resulted in 366 AF demagnetized specimens. Thermal demagnetization was applied to 103 layers sparsely distributed along the section, which resulted in 162 thermally demagnetized specimens. Representative examples of thermal and AF demagnetization data are shown in Figure 2.

The thermal demagnetization efficiently removed all the remanent magnetization by 600 °C and revealed two components of magnetization: one (secondary) removed at temperatures below 350 °C and the other (characteristic) with high unblocking temperatures between 350 and 600 °C. Specimens DD8A1B and DDL078B2B shown in Figure 2 are examples of thermal demagnetization that represent the typical behavior of Mafra specimens. DDL078B2B is an example of a pilot group of thermal demagnetization, containing more than 30 steps of demagnetization, and DD8A1B is an example of specimens that were subjected to a simpler protocol, with fewer demagnetization steps. Both specimens show good discrimination of the two components of magnetization, which are separated by a cusp elbow in the orthogonal plot. The final steps of demagnetization (between 350 and 600 °C) are well grouped in the stereographic projection and are distributed along a direction centered on the origin of the orthogonal plot. For temperatures higher than 600 °C, the remanence presents low values in the intensity plots and random behavior in the stereographic projection, and plots near the origin in the orthogonal plots, attesting to the complete demagnetization.

The decay of intensity of remanence was smooth for AF steps from 0 to 100 mT, but for the last steps (with about 10% of the intensity remaining), the behavior was unstable. The remanent magnetization data are distributed along a great circle between the first and last (by 10 mT) steps of demagnetization for almost all

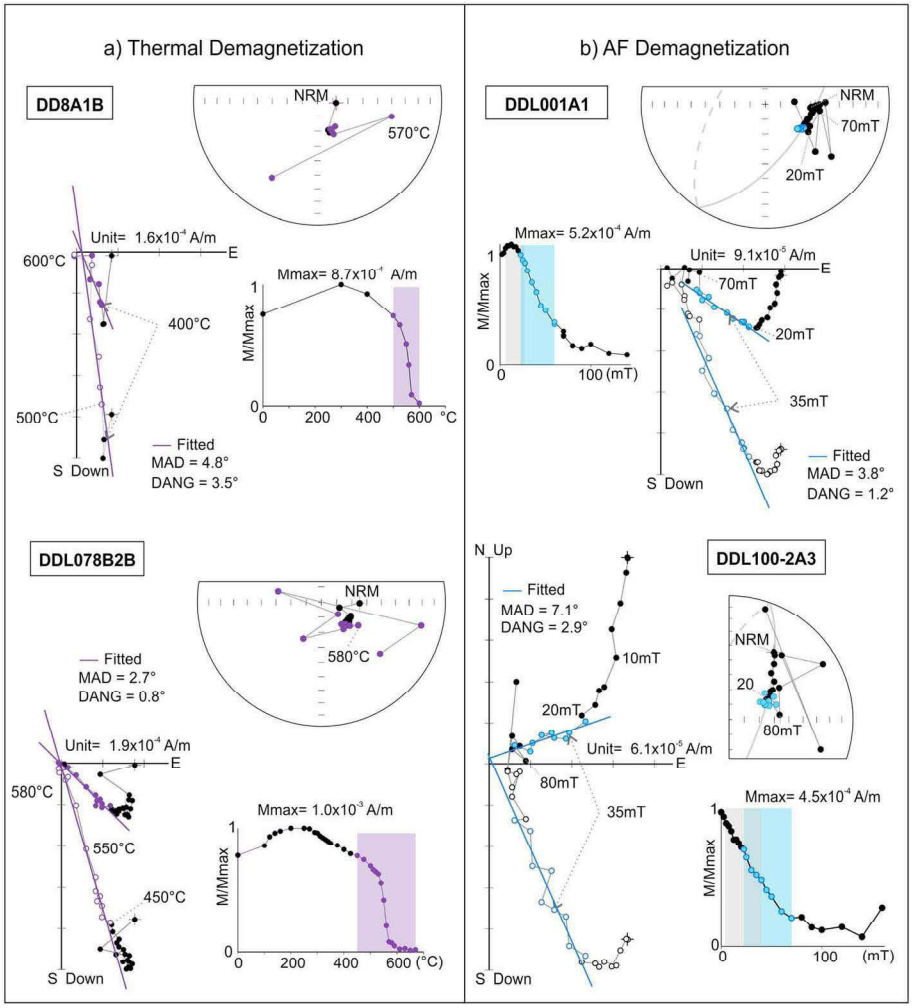

Figure 2. Intensity curves, orthogonal plots, and stereographic projections of four examples of Mafra demagnetized specimens. Alternating field (AF; thermal) demagnetizations are on the right (left). Orthogonal plots are composed of horizontal projection (filled circles) and vertical projection (empty circles). Filled circles in stereographic projections represent positive inclinations. The chosen steps for calculating the characteristic thermal and AF-C directions are colored in purple and blue, respectively, in the orthogonal, stereographic, and intensity plots. The great circles were fitted using the range shown in the grey area in the intensity plot. The great circles are shown in the stereographic plots. The maximum angular deviation (MAD) and the deviation angle between the center of mass and the fitted direction (DANG; Tauxe, Banerjee, et al., 2016) are also shown.

samples. This behavior is shown by stereographic projections of AF examples of Figure 2. The specimen DDL001A1 is an example that reveals the presence of two components, one of low coercivities up to 20 mT and the other along the range from about 25 to 70 mT; above 70 mT the data present a random behavior (intensity, orthogonal, and stereographic plots). The specimen DDL100-2A3 also shows the presence of two components, but it presents a smoother curve instead of two well-defined lines, and the same randomness toward the end of demagnetization. Excluding these noisy data at the end, the demagnetization for the more coercive range tends to go to the origin of orthogonal plot (see straight lines on Figure 2b).

Principal component analysis (Kirschvink, 1980) was used for fitting components of thermal and AF data. Part of the AF demagnetization data was also subjected to great circle adjustments (Halls, 1976). The secondary components were identified in the range of low coercivities (0 to 15 mT) and low temperatures (up to 350 °C) for 314 (232 AF and 82 thermal) specimens. The maximum angular deviation (MAD) varied from 0.5° to 26.3°. The high unblocking temperature characteristic component (Th-Ch) was fitted in the range of 350 to

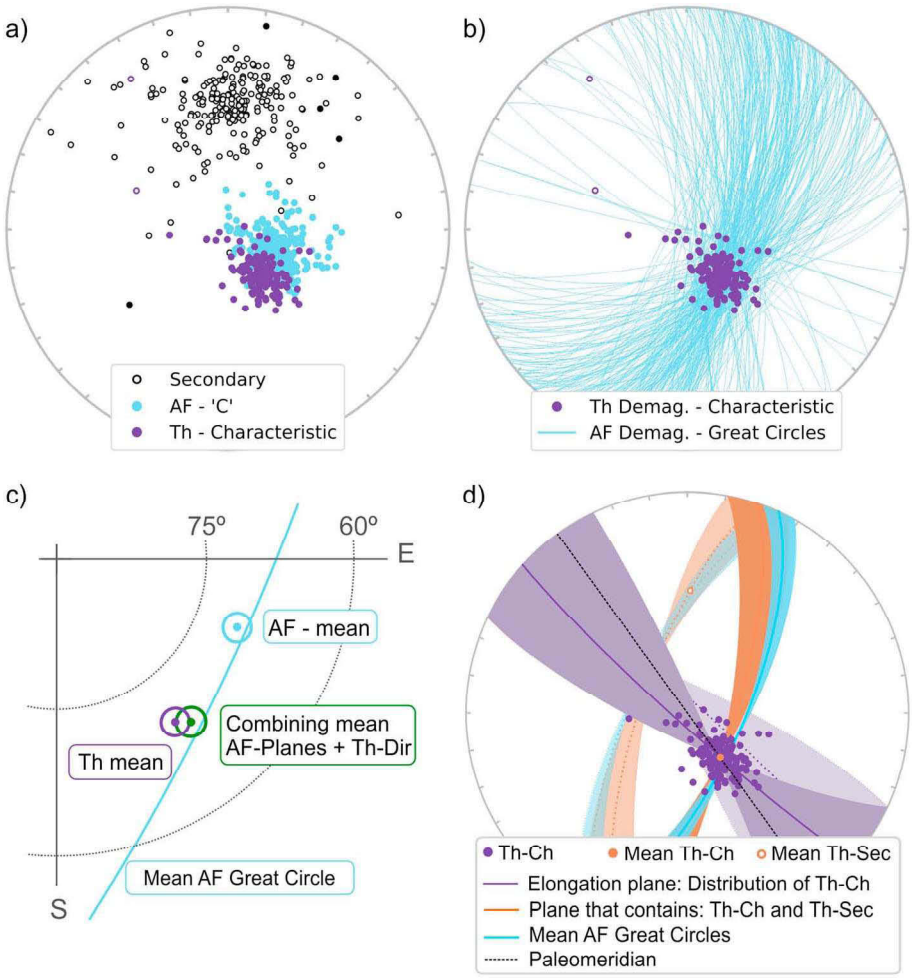

Figure 3. Directions and planes determined for demagnetized specimens from Mafra Formation. (a) Stereogram projection with secondary directions in black, characteristic component (thermal demagnetization data) in purple and C component (alternating field [AF] demagnetization data) in blue circles. Empty (full) circles are negative (positive) inclination. (b) Only lower projection of planes identified from AF demagnetization data (great circle analyses; Halls, 1976) and characteristic components determined by thermal demagnetization. (c) Global means using thermal data (purple), mean of C component, and mean of great circles from AF data (blue), and combining AF planes and Th directions (green). (c) The purple line represents the plane that contains the maximum and intermediate eigenvalues (τ_1 and τ_2) from the "orientation matrix" T (Scheidegger, 1965) from characteristic thermal data (Th-Ch). It indicates the plane of elongation. The orange plane is the plane that contains the mean thermal secondary (orange circle with negative inclination) and the mean characteristic thermal direction (orange circle with positive inclination). The blue plane is the mean great circle of AF data. The limits were defined by 1,000 bootstrap resamplings. The black dashed line is the direction of the paleomeridian given by the declination of thermal mean.

600 °C for the majority of the specimens. Only four specimens (2.5%) showed random behavior and gave no reliable components. The MAD of the Th-Ch components varied from 1.4° to 25.4°. The high-coercivity characteristic component (AF-C) was identified in the range of 35 to 100 mT, excluding the noisy last steps. The values of MAD of AF-C components varied from 1.7° to 32.1°. The AF great circles were determined in the range of 5 to 100 mT. A total of 322 planes were defined, and MAD values varied from 1.4° to 31.4°. Directions or planes with MAD higher than 15° were rejected for future analyses. This data cut represents about 11% of the total data set. All 954 components and planes with MAD $\leq$ 15° from Mafra rocks are shown in Figure 3 and are listed in Table S1 (in the supporting information).

The secondary components form a relatively highly dispersed group pointing to the north with negative inclinations, which is compatible with the present geomagnetic field in the area. The AF-C and Th-Ch components point to the southeast and have high positive inclinations, excepting six results (two from thermal

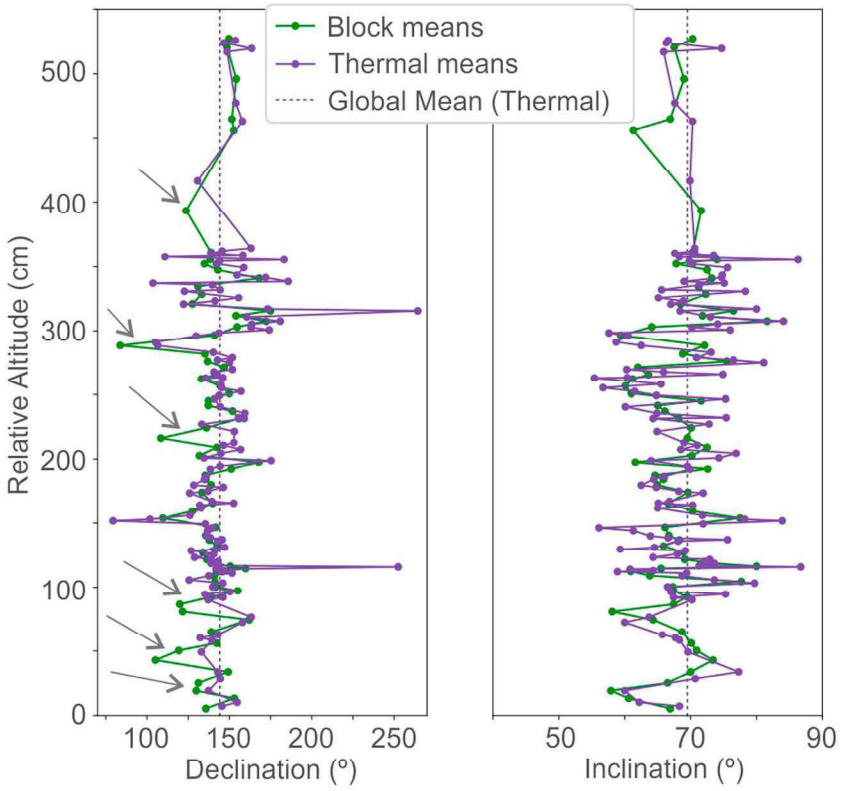

Figure 4. Declination and inclination of mean directions of groups of thermal directions and alternating field (AF) planes (green) and thermal mean directions per layer (purple). Arrows indicate the systematic differences of lower declination for block means (combining of AF-planes and Th-Ch).

and four from AF demagnetizations) with negative inclinations. These are spurious directions because they have no consistency with nearby samples.

Although the AF-C and Th-Ch point to a similar direction, they are systematically different from each other (Figure 3a); the AF-C directions present visibly lower declinations than Th-Ch. Figure 3c further shows that the global averages with only Th-Ch (purple) and only AF-C (blue) are quite different from each other, the angular cones of 95% confidence do not intercept and are small (both 1.4°) when compared to the angular distance between the vectors (11°). The mean AF-C plots in between the Th-Ch and the secondary means (Figure 3c), in the same remagnetization plane, therefore, indicating an incomplete removal of the secondary magnetization.

The fitted planes of AF demagnetization data (AF-planes) seem to be more consistent with thermal data because of the region in the stereographic projection where most of the intersections lie in the same region that is occupied by Th-Ch directions (Figure 3b). When they are grouped using the method of grouping planes and directions with constraints (McFadden & McElhinny, 1988) using groups of at least five specimens along the stratigraphy, they present a global mean (green, in Figure 3c) that plots between the thermal mean and the mean remagnetization plane, with only a partial superposition of α_{95} (grouping global mean: dec = 140.5°, inc = 68.8°, α_{95} = 1.5°, N = 71 groups; thermal global mean: dec = 143.9°, inc = 69.8°, α_{95} = 1.4°, N = 118 layers). The differences appear more striking when we see the plot of both data sets along the relative elevation (Figure 4). At some levels, the declination of grouped directions (green) are very different from thermal directions (purple) and repeatedly tend to smaller declinations (indicated by arrows in Figure 4). Because of these systematic differences, the only partial overlapping of α_{95}, and the positioning of the blocking mean between the remagnetization plane and the thermal mean, we consider it likely that even using only the analyses of AF data by the great circle fitting and grouping method will contaminate the results with incomplete removal of secondary directions. Thus, in the following, we considered only the thermal data set (Table S2) to avoid any contribution of secondary components in the final results.

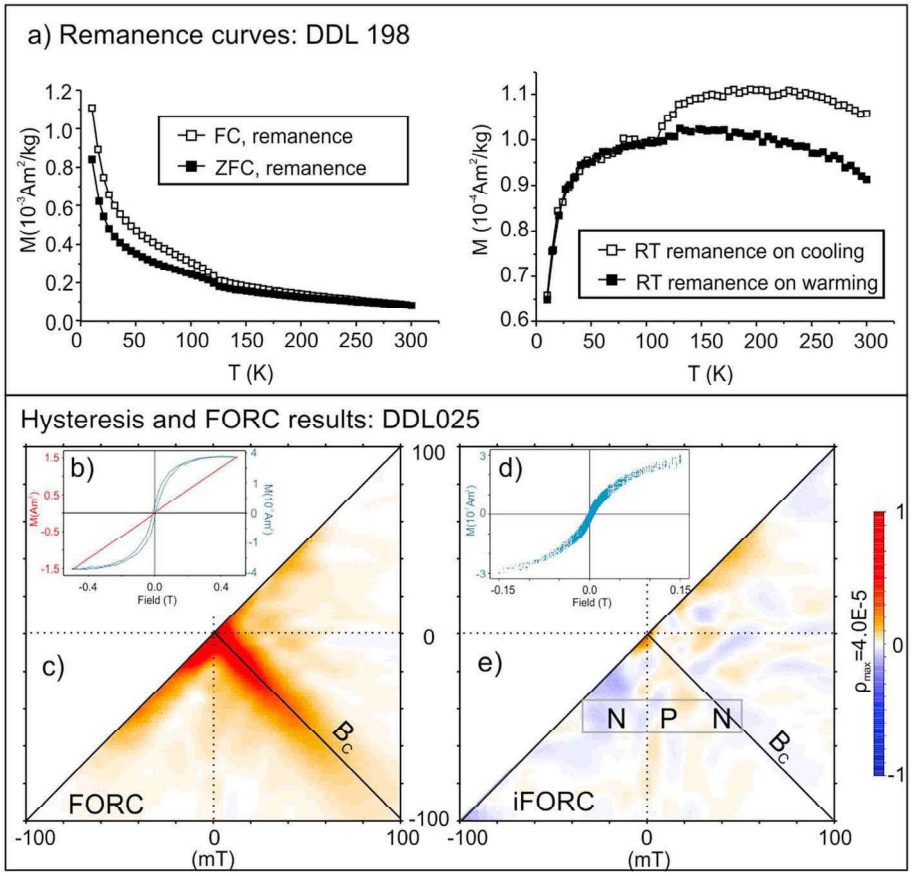

Figure 5. Rock magnetic results: (a) Remanence curves of sample DDL198: Field cooling (FC) and zero field cooling (ZFC) curves on left and room temperature (RT) curves on the right. Bottom: Irregular first-order reversal curves diagrams for sample DDL025. (b) A cycle of hysteresis with and without paramagnetic correction; (c) conventional first-order reversal curve (FORC) diagram; (d) corrected hysteresis cycles; (e) induced FORC diagram. The rectangle with N, P, and N is showing characteristic triple negative-positive-negative that is common for samples that contain single domain particles. Smoothing factor 5, 120 FORC curves were measured, with 300 ms of averaging time, maximum field of 300 mT and saturation field of 300 mT.

Figure 3d shows the remagnetization planes defined by thermal data (orange) determined by the plane that contains the secondary and characteristic mean directions and by AF data (blue) determined by the mean great circle. The remagnetization planes determined by thermal and AF data are compatible with one another, and the elongation plane is totally different from them. As the elongated shape of the characteristic thermal directions (purple line at Figure 3d) is not compatible with the remagnetization planes, we can discard the hypothesis that this shape of distribution is due to incomplete removal of the secondary direction. Moreover, as the elongation plane is compatible with the plane that contains the paleomeridian and vertical, the elongated shape of the Mafra distribution is not related to inclination shallowing effect.

5. Rock Magnetism and Flattening Factor *f* Determination

The samples presented a transition in room temperature remanence cooling curves at around 120 K and a partial recovery of the remanent magnetization during heating. This transition is called the Verwey transition (Dunlop & Ozdemir, 1997) and indicates the presence of magnetite. FC remanence curves of all samples presented higher values than the ZFC remanence, which is indicative of the presence of single domain magnetite [following Bilardello & Jackson, 2013]. Figure 5a shows one typical example of FC, ZFC, and room temperature remanence curves (sample DDL198).

Irregular FORCs at room temperature were performed on three selected samples from Olsen quarry to confirm the domain structure of the magnetic carrier. The conventional FORC diagram for all analyzed samples

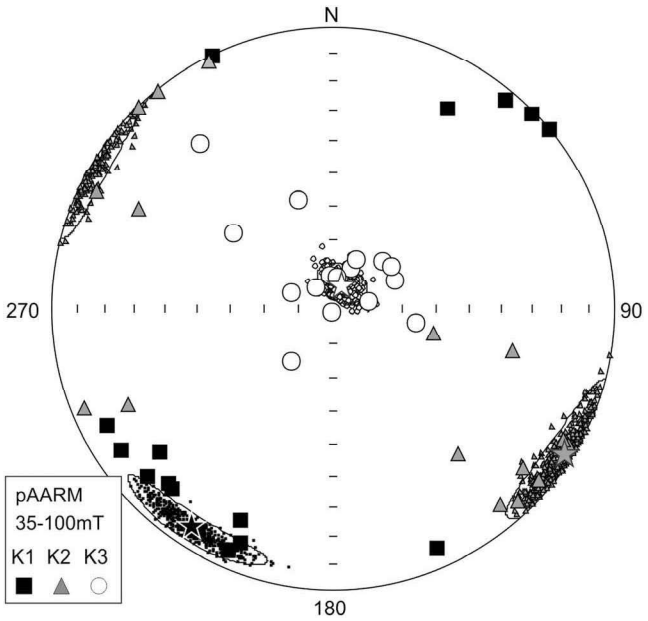

Figure 6. Equal-area projection of principal of anisotropy of partial anhysteretic remanent magnetization (pAARM) tensors axis: K3 (minimum, circle), K1 (maximum, square), and K2 (intermediate, triangle). Small symbols are 500 bootstrapped mean tensors axis, big symbols are the tensor for each sample, and stars are the mean tensor. The ellipses are 95% of bootstrapped confidence region.

showed a positive distribution on the Bc axis (see DDL025 on Figure 5b). Induced FORC diagrams exhibited a characteristic triple negative-positive-negative that is common for samples that contain single domain particles, following Hu et al. (2018) and Zhao et al. (2017).

Sixteen specimens distributed along the sampling section were selected for AARM measurements to define a mean K_A tensor that represents the rock unit, following Kodama (2009). Partial AARM acquisition was conducted in the range 35 to 100 mT of AF field with a bias field of 0.1 mT. This range corresponds to the range of AF demagnetization that had the least influence on secondary magnetization (see Figure 2).

Results of AARM for each specimen, mean ellipsoid (with bootstrapped confidence ellipses), and 500 bootstrapped means are shown in Figure 6, where K_{A1}, K_{A2}, and K_{A3} are the axes of the eigenvectors of, respectively, maximum, intermediate, and minimum eigenvalues of the K_A tensor. The results have approximately the same behavior, where the majority of maximum and intermediate directions (K_{A1} and K_{A2}) are near to the horizontal and minimum axes (K_{A3}) are close to the vertical. The anisotropy degree of each specimen varied between 1.5% and 5.5%. The mean ellipsoid (large symbols) presents an oblate shape and is positioned parallel to the horizontal. The normalized mean tensor K_A has eigenvalues of $K_{A1} = 1.013$, $K_{A2} = 1$, $K_{A3} = 0.987$, with the directions $Dec_{K1} = 212.7$, $Inc_{K1} = 7.4$, $Dec_{K2} = 122.4$, $Inc_{K2} = 1.8$, $Dec_{K3} = 19.1$, $Inc_{K3} = 82.4$.

The AARM and rock magnetic results allowed us to determine the inclination shallowing correction factor (flattening factor, f). Magnetite can have particle anisotropy a from 1 (isotropic particles) to infinite (elongated uniaxial). According to Dunlop and Ozdemir (1997), elongated particles should not exhibit the Verwey transition, which means that the Mafra's remanence curves are attesting to the presence of magnetite, but not the elongated particles. However, we can not discard the presence of elongated particles, because of the bulk remanence anisotropy, despite the low degree of anisotropy, agrees with the expected fabric for sedimentary rocks (horizontal oblate elipsoid on Figure 6). The flattening factor is determined by $f = K_{A3}(a+2) - 1/K_{A1}(a+2) - 1$ (Jackson et al., 1991), where K_{A3} and K_{A1} correspond to the minimum (vertical) and maximum (horizontal) axes from K_A tensor and a is the particle anisotropy that for natural magnetite has a typical value of $a = 2$ (Kodama, 2012). Because the difference between the K_{A3} and K_{A1} from the mean Mafra tensor is small (1.013 and 0.987, respectively), the flattening factor would vary between 0.96 and 0.97 for any value of a between 1 and infinite. Therefore, for Mafra results, the particle anisotropy does not affect significantly the final flattening factor estimative. Anyway, considering the typical value of $a = 2$, the resulting flattening factor for Mafra rocks is $f = 0.97$, which means almost no correction.

6. Cyclostratigraphic Results

There are patterns strongly suggestive of astronomical signals in the χ and ARM series. A ~60-cm cycle occurs throughout both data series (Figures 7c and 7d, purple arcs); between 100 and 150 cm, the cycle is shortened to 30 cm (down-pointing purple arrows). This cycle is prominent in the power spectra of both χ and ARM series (Figure 8); the spectral peak with a wavelength of 65 cm exceeds the 99% confidence level for red noise in the ARM spectrum. In Figures 7c and 7d, other shorter cycles occur within the ~60-cm cycles, preferentially at 23 and 10.6 cm in the χ spectrum and at 13 cm primarily in the ARM spectrum (Figures 8c and 8d). This overall pattern suggests that the 65-cm cycle may represent the 100-kyr short orbital eccentricity cycle. The wavelength ratio 65:23:13:10.6 = 6.13:2.17:1.23:1 is not far from the ratio of Late Carboniferous astronomical periodicities of Berger and Loutre (1994): 100:34.2:20.7:17.4 = 5.75:1.97:1.19:1. Moreover, the 60% "loess" curves of the χ and ARM series have a cycle with a ~270-cm wavelength (Figures 7a and 7b), that is, at a scale suggestive of the 405-kyr long orbital eccentricity cycle (65 cm × 4.05 = 263.25 cm). The FFT spectrograms (Figure 8) show a sharp shift of frequencies to the right at ~70–100 to 150 cm, suggesting a decrease in sedimentation rate in this stratigraphic interval and explaining the wide

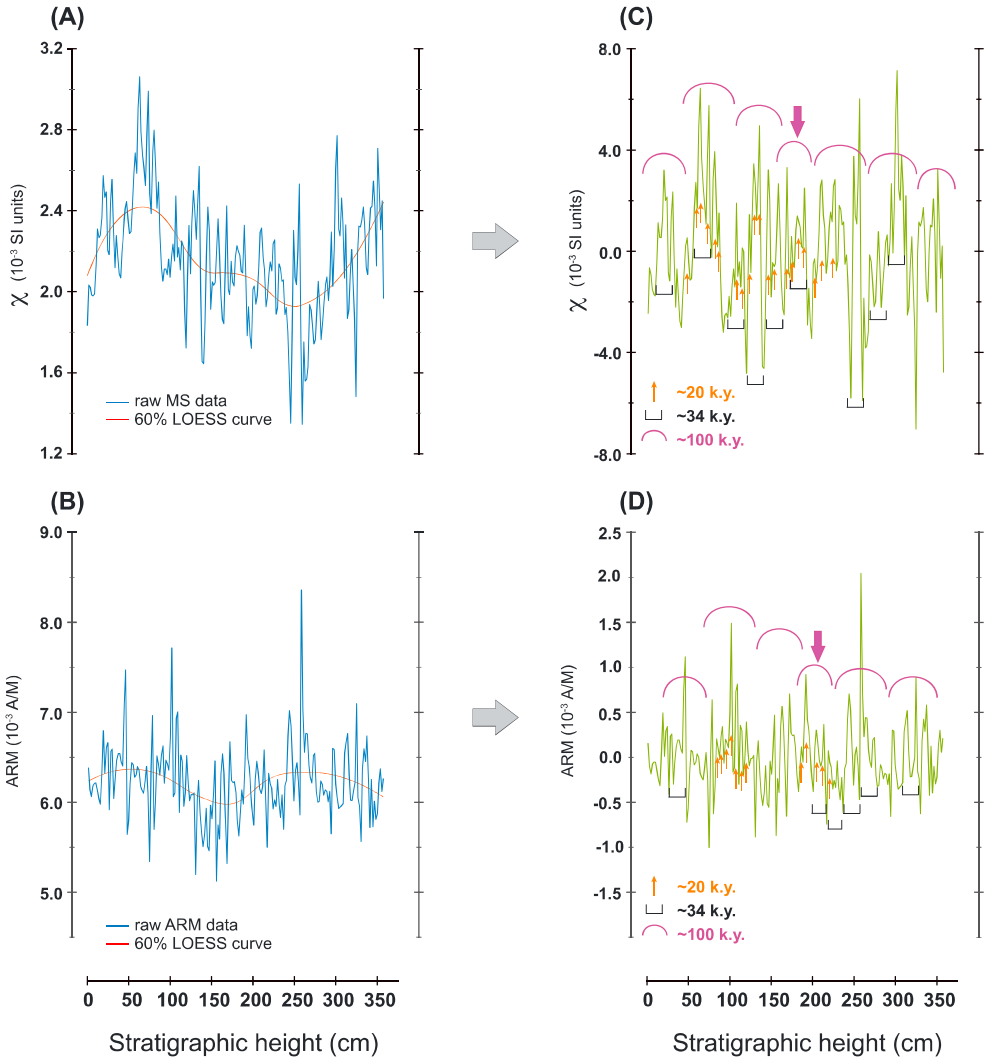

Figure 7. The cyclostratigraphic series. (a) Raw magnetic susceptibility (χ) and (b) raw anhysteretic remanent magnetization (ARM) data series after linear interpolation and resampling (blue) and their corresponding 60% "loess" curves (red). (c) χ and (d) ARM data series after removal of the 60% loess curves. Purple arcs = 100-kyr short orbital eccentricity cycles, black brackets = 34 kyr obliquity cycles, and upward pointing orange arrows = 20 kyr precession index cycles.

range of wavelengths presumably related to the precession index (12.9, 7.8, and 6.2 cm in the ARM spectrum and 10.6, 7.3, and 6.5 cm in the χ spectrum).

Assuming that the 65-cm cycle is the main expression for the ~100-kyr short orbital eccentricity implies a sedimentation rate of 65 cm/100 kyr = 0.65 cm/kyr for the series. Thus, the 360-cm series length may represent a duration of 360 cm/(0.65 cm/kyr) = 553,846 years, and a 1-cm-thick specimen would be expected to average over 1.5 kyr. As the total section of paleomagnetic sampling comprises 5.3 m, the complete sampled DDL section may correspond to a duration of ~530 cm/(0.65 cm/kyr) = 815,385 years.

7. Mafra and Other South American Paleomagnetic Poles

The remanent magnetization of the Mafra rocks has high positive inclination and is carried mainly by single domain magnetite as revealed by thermal demagnetization. No other magnetic carrier was identified, but this does not exclude the possibility of a small contribution of a secondary mineral carrying the secondary direction, although not detected. The weak anisotropy indicates only a very small correction for inclination shallowing effect (flattening factor f = 0.97), which changes the final mean inclination by 0.5°. The 118

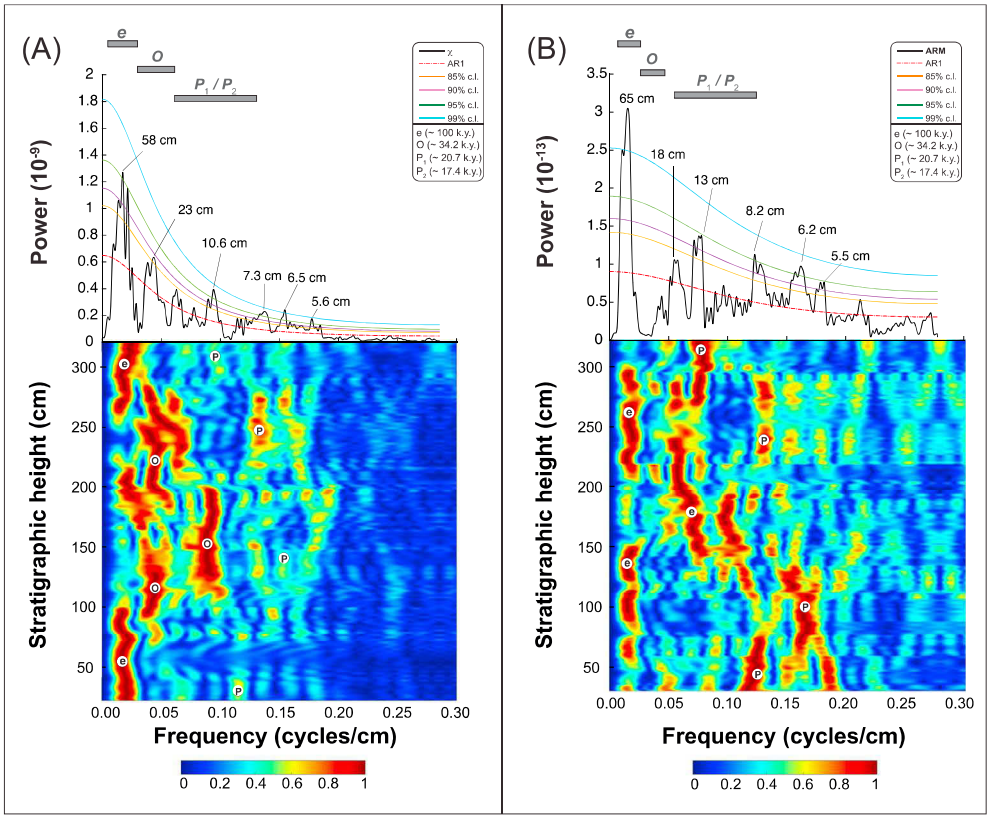

Figure 8. Spectral analysis of the cyclostratigraphic series for (A) χ and (B) anhysteretic remanent magnetization (ARM). Top: 2π multitaper power spectra, with the AR(1) red noise spectral model and 85%, 90%, 95%, and 99% confidence levels (c.l.) for null hypothesis testing. Wavelengths of spectral peaks are labeled in cm. Bottom: Evolutionary fast Fourier transform (FFT) spectrograms with a 75-cm sliding window, with each calculated FFT spectrum normalized to 1; e, O, and P indicate ~100-kyr short orbital eccentricity, obliquity, and precession, respectively.

results (Table S2) were converted into VGPs, and a variable cutoff angle procedure (Vandamme, 1994) was used for selecting data. The final cutoff angle was of 24.8°, which removed seven sites.

The mean direction of characteristic remanent magnetization of Mafra rocks, using only the selected directions, is Dec = 144.2° and Inc = 69.0° (N = 111, R = 110.1, k = 129.1, α_{95} = 1.2°), which results in a paleolatitude of 52.4°S. The mean direction with inclination shallowing correction (f = 0.97) changes to Dec = 144.2° and Inc = 69.5° (N = 111, R = 110.2, k = 134.4, α_{95} = 1.2°) with paleolatitude of 53.2°S. The final Mafra PP position is 51.9°S, 344.3°E (N = 111, R = 109.0, K = 55.9, A_{95} = 1.8°). Mafra PP (number 16 in Table S4) is plotted as a star in Figure 9a. The Mafra PP without inclination shallowing correction (named as 16.1 in Figure 9a) is practically the same as the corrected one (16.2). The confidence circle of 95% (A_{95}) for the Mafra pole is almost the symbol size and not easily distinguished in the figure.

The set of PPs plotted in Figure 9 and listed in Table S4 from the supporting information was based on the compilation done by Domeier et al. (2012) and some new results from Ernesto et al. (2015), Franco, Ernesto, et al. (2012), and Yokoyama et al. (2014). Poles from 9 to 19 are reverse polarity and are assigned to the Kiaman superchron interval [~318 to 262 Ma; Opdyke & Channell, 1996]. The PP 18 (Pular and Cas Formations), which have mixed polarities, including a normal polarity record, which, according to Jesinkey et al. (1987), represents a normal event at the base of Kiaman superchron. Mafra PP is inserted in the A_{95} cone of confidence from poles Pular and Cas Formations PP (number 18) and La Tabla Formation PP (number 19). Those poles are from igneous rocks from Chile (Jesinkey et al., 1987) and have similar ages.

The stratigraphic correlation between the Mafra and Rio do Sul formations is well constrained in Santa Catarina State. The Rio do Sul Formation positions in the upper portion of Itararé Group and Mafra

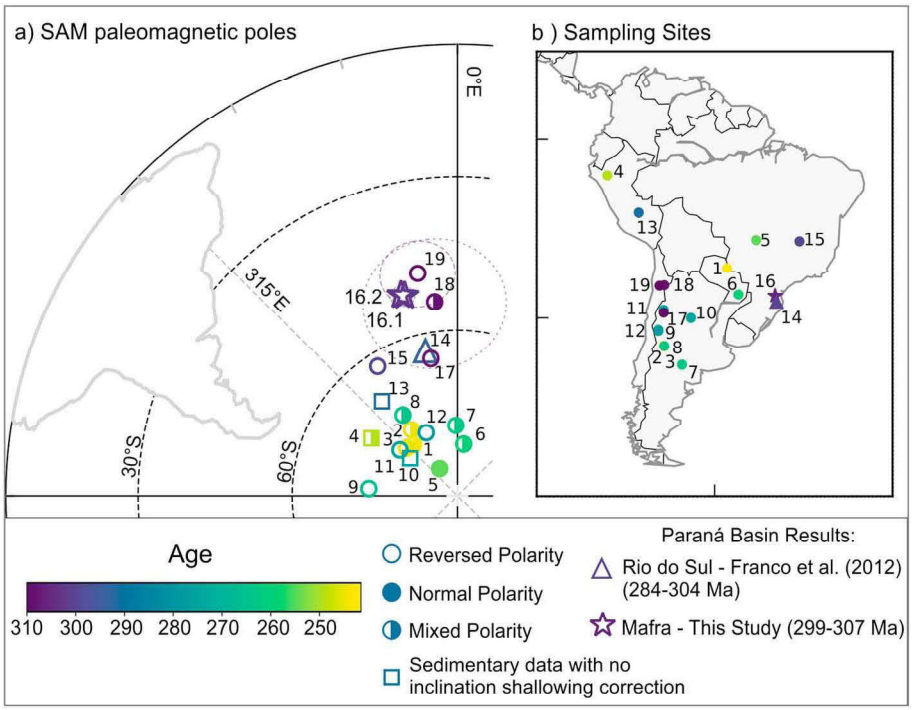

Figure 9. South American paleomagnetic poles. (a) Paleomagnetic poles positions of ages from Carboniferous to Triassic times, where 1-Ernesto et al. (2015); 2, 3, 8-Domeier, Van der Voo, Tomezzoli, et al. (2011); 4-Gilder et al. (2003); 5-Yokoyama et al. (2014); 6-Rapalini et al. (2006); 7-Domeier, Van der Voo, Tohver, et al. (2011); 9, 12-Rapalini and Vilas (1991); 10, 11-Geuna and Escosteguy (2004); 13-Rakotosolofo et al. (2006); 14-Franco, Ernesto, et al. (2012); 15-Brandt et al. (2009); 16-this study; 17-Geuna et al. (2010); 18, 19-Jesinkey et al. (1987). The numbering follows the sequence from Table S4 (supporting information). The corrected (16.2) and uncorrected (16.1) Mafra paleomagnetic pole are plotted as stars. The Rio do Sul pole (Franco, Ernesto, et al., 2012) is plotted as a triangle. Empty, full, and half-full symbols are referred to exclusively reversed, exclusively normal, and mixed polarity, respectively. The sedimentary and volcaniclastic results that were originally corrected for the inclination shallowing effect by the authors are plotted in Figure 9a (poles 3, 14, and 15). The sedimentary poles that did not have any correction are also plotted (squares, PPs number 4, 10, and 13). (b) Site positions of the paleomagnetic poles (following the same numbering, color scale, and type of symbols).

Formation in the middle portion, following the definition of Schneider et al. (1974). As already mentioned in section 2, the age of the Mafra formation is late Pennsylvanian (Kasimovian to Gzhelian). The Rio do Sul formation is younger and corresponds to the Permo-Carboniferous boundary (Gzhelian to Sakmarian, ~ 284.4 to 303.9 Ma). Recent dating based on Rb-Sr of the base of this unit (Lontras shale) indicates a minimum age of 287 ± 10 Ma (Koester et al., 2016). Conversely, Cagliari et al. (2016) put some more constraints on the ages of these formations as they place the topmost glacial deposits of the Itararé Group at 307.7 ± 3.1 Ma (Kasomovian-Moscovian), therefore placing the Rio do Sul and Mafra formation being slightly older than this.

The paleomagnetic pole from the Rio do Sul Formation Franco, Ernesto, et al. (2012) is plotted as a triangle and is almost equal to the PP 17 [La Colina pole from Geuna et al., 2010] observed from both sedimentary and volcanic rocks. The Rio do Sul PP would produce a magnetic inclination at Mafra site of 63.9° corresponding to a paleolatitude of 45.6°S. This implies a velocity of 3.4 cm/year toward the north (considering a maximum age difference of ~20 Ma; the lowest limit of age from Mafra and the upper limit of age from Rio do Sul) and a velocity of about 6.4 cm/year. This result is compatible with the velocities of about 6 cm/year northward between 310 and 290 Ma determined by Torsvik et al. (2012) for Gondwana Supercontinent. After this time interval, the general trend of displacement of Gondwana supercontinent is northward, and the younger paleomagnetic poles gradually plot at higher latitudes, heading toward the geographic pole. After the Pangea breakup, the paleomagnetic poles for the South American plate remained at higher latitudes (Ernesto, 2005 and Font et al., 2009), which means that there is no possibility of the paleomagnetic direction determined by Mafra rocks be a younger overprint.

Field tests such as folding or conglomerate tests might reinforce the primary origin of the magnetization, but none is available for this intracratonic basin. This absence does not mean that the magnetization is not primary. These sediments exhibit no signs of tectonic folding and were certainly not remagnetized by folding effects. Therefore, we consider the characteristic component, identified by thermal demagnetization, as a primary magnetization.

8. The Record of Paleosecular Variation by Mafra Rocks Compared to GGP Models

The positive-inclination remanent magnetization of the Mafra section is expected for a primary magnetization, as its age is entirely constrained in the Kiaman superchron interval [~318 to 262; Opdyke & Channell, 1996]. According to the cyclostratigraphic analysis (section 8), the Mafra studied section covers more than 800 kyr, which ensures a representative sampling of the paleosecular variation. Moreover, the variation of the characteristic magnetization along the stratigraphic sequence does not show any tendency from bottom to top that could be related to age differences (see Figure 4). Considering the long period represented in the deposition of these sediments, the dense sampling of this section, the primary nature of its magnetic remanence, and the small correction of inclination shallowing applied (AARM procedure), we can consider it a reliable and detailed record of a section of the Kiaman geomagnetic field. However, the Mafra record should be considered as a smoothed signal from the geomagnetic field variations, due to the low rate of deposition of the studied section (~800 kyr for 5.3 m); each sedimentary layer represents a time-averaged field of some thousands of years. Therefore, this paleomagnetic data set cannot be considered as a spot reading of the geomagnetic field, and a partial smoothing of geomagnetic variation is anticipated.

Figure 10a shows the resulting distribution of magnetic remanent directions (mean direction per stratigraphic layer) with the expected direction (Dec = 144.3°, inc = 69.3°) rotated to the origin (center of stereographic projection). The elongation values with the 95% bootstrap confidence limits are $E_{\mathrm{M}} = 2.08^{3.03}_{1.45}$ for noncorrected Mafra directional data and $E_{\mathrm{M}i} = 2.08^{3.13}_{1.44}$ for AARM-corrected data (inclination shallowing correction). The declination of V_2 (eigenvector associated to intermediate eigenvalue τ_2 of T) with the 95% bootstrap confidence limits is $\mathrm{Dec}_{V2} = 128.5^{148.0°}_{114.4}$, which is compatible with the mean declination (direction of paleomeridian), as predicted by TK03.GAD model. However, the value of elongation is higher and incompatible with that predicted, and the 95% confidence bound does not intercept the TK03.GAD elongation curve (black dashed line in Figure 10f). As the value is greater than predicted by the model for its inclination value and the elongation is along the paleomeridian direction, there is no flattening correction that recovers an elongation/inclination pair that makes Mafra data set compatible with TK03.GAD model. Moreover, this would be an inappropriate procedure since the data were already corrected by AARM method.

The dispersion of VGPs of the Mafra Formation with 95% bootstrap confidence limits was $S_{\mathrm{M}} = 11.0°^{11.9}_{9.9}$ for uncorrected data and $S_{\mathrm{M}i} = 10.9°^{11.8}_{9.8}$ for AARM-corrected data. As we can see in Figure 10g (purple star), this result is lower than that predicted by TK03.GAD (black dashed line, Figure 10g). This result is not surprising as the TK03.GAD model is related to the last five million years when the geomagnetic field shows higher reversal rates, quite different from the behavior during a superchron. We also need to consider that the reduction of scatter can be enhanced by smoothing of the geomagnetic signal implied by the low deposition rate of Mafra rocks. Even so, other paleomagnetic results (both igneous and sedimentary data) from Kiaman times also presented a reduced secular variation for low and medium paleolatitudes. The VGP scatter of intrusive rocks of Oslo Graben (Haldan et al., 2014) and lavas of Bakaly Formation (Bazhenov et al., 2016) are examples of more two different types of rock that recorded the reduced behavior of the paleosecular variation during the Kiaman superchron (dispersion plots are shown in Figure 10g). Moreover, a recent compilation of paleomagnetic data from Kiaman times shows a strong paleolatitudinal dependence of the dispersion (de Oliveira et al., 2018).

The paleomagnetic data sets are usually limited to some tens of sites, and as the elongation is a ratio of two variables, it has a wide probability distribution with higher variance. Therefore, the elongation results commonly have large error bars, even for the longest sections of paleomagnetic data. The number of sites must be high to define this parameter better. Tauxe et al. (2008) recommended more than 100 paleomagnetic sites.

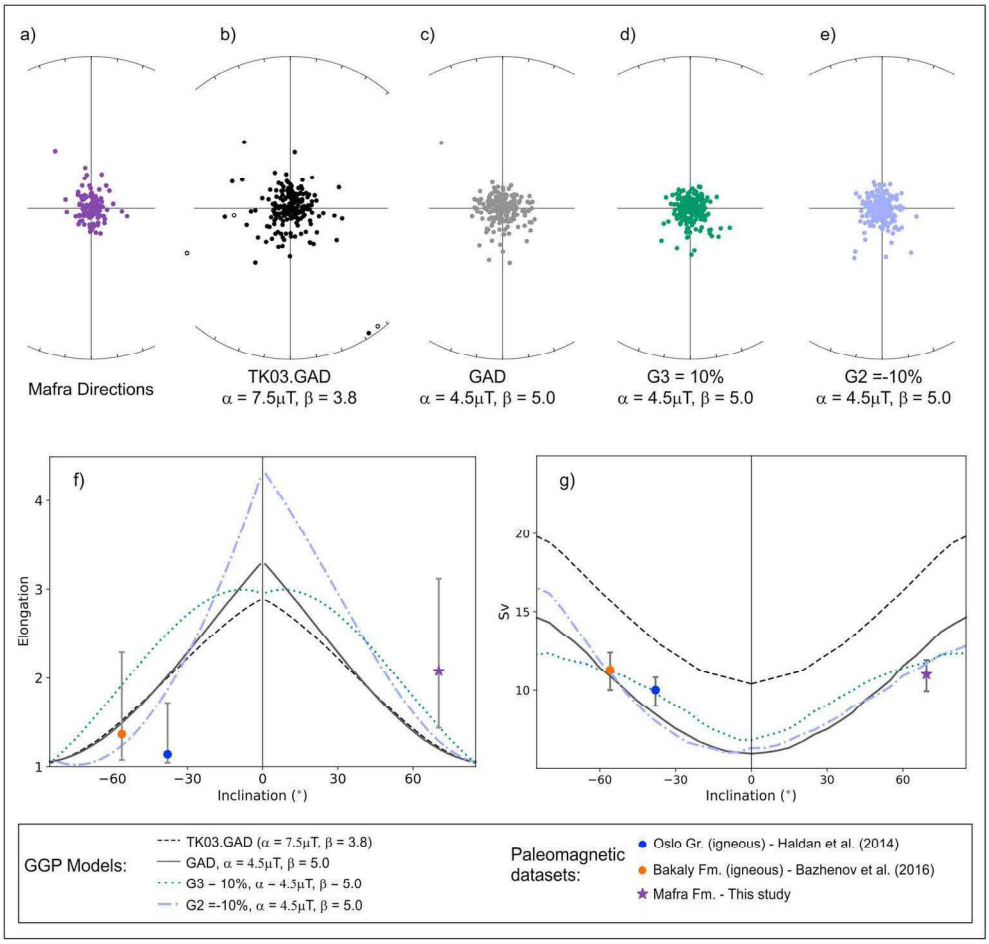

Figure 10. Paleosecular variation from Mafra Formation and Giant Gaussian Process (GGP) models simulations: (a) Mean direction per stratigraphic layer distribution of Mafra Formation, with the expected direction rotated to the origin of stereographic projection; (b) directions of 200 simulations of TK03.GAD model for the same expected inclination ($i = 69.3°$); (c) directions of 200 simulations of a modified version of TK03 model with lower α parameter ($\alpha = 4.5$ μT) and higher β parameter ($\beta = 5.0$) for the same expected inclination ($i = 69.3°$); (d) the same as (c), but with nonnull octopolar contribution of 10% (G3 = 0.10); (e) the same as (c), but with a nonnull quadrupolar contribution of −10% (G2 = −0.10); (f) elongation of the longest data sets from Kiaman period: purple star denotes this study, blue circle denotes Oslo Graben lavas (Haldan et al., 2014), and orange circle denotes Bakaly Formation (Bazhenov et al., 2016); these results are in Table S5. The curves are elongation results from 10,000 of simulations of GGP models: black dashed line is the original TK03.GAD, fitted polynomial is $E(I) = 3.160 \times 10^{-6}|I|^3 - 3.525 \times 10^{-4}|I|^2 - 1.466 \times |I| + 2.895$, from Tauxe et al. (2008), the black continuous curve is TK03.GAD model with $\alpha = 4.5$ μT, $\beta = 5.0$, fitted polynomial is $E(I) = 2.426 \times 10^{-6}|I|^3 - 1.385 \times 10^{-4}|I|^2 - 3.236 \times 10^{-2}|I| + 3.318$, green dot line has $\alpha = 4.5$ μT, $\beta = 5.0$, and 10% of octopolar contribution, fitted polynomial is $E(I) = 4.638 \times 10^{-6}|I|^3 - 8.011 \times 10^{-4}|I|^2 + 1.213 \times 10^{-2}|I| + 2.947$, light-purple dash-dot line has −10% of quadrupolar contributions fitted polynomial is $E(I) = -1.038 \times 10^{-6}I^3 + 4.426 \times 10^{-4}I^2 + 8.322 \times 10^{-2}I + 4.335$, for $I \leq 0$ and $E(I) = 4.505 \times 10^{-6}I^3 - 3.777 \times 10^{-4}I^2 - 3.919 \times 10^{-2}I + 4.348$, for $I > 0$. Simulation results and parameters from these models are in Table S6. (g) Dispersion of virtual geomagnetic poles corresponding to 10,000 simulations of GGP models using the variable cutoff. The colors and line styles follow the same pattern as (f).

The longest igneous sections of paleomagnetic records for Kiaman times are the other two paleomagnetic results shown on Figure 10. The Oslo Graben results (blue circle) are based on 104 paleomagnetic sites, and Bakaly Formation results (orange circle) have 88 paleomagnetic sites. Although their reduced dispersions are in agreement with Mafra result, the elongation results are smaller than the TK03.GAD elongation prediction. The Bakaly Formation mean result plots near the elongation curve predicted by TK03, and considering its error bars, it is compatible with the model. The Oslo Graben result plots far from the model curve

(almost circular distribution), and its bootstrap confidence limits do not intercept the model curve. The elongation values were obtained with the whole of the available directional data set, without any cutoff, in order to preserve the number of sites.

The GGP model curve is built from the elongation/dispersion results of 10,000 simulations and are not theoretical values. This implies an intrinsic uncertainty contained in the model. As we do not have a direct determination of a theoretical elongation or VGP scatter, in this work, as in other studies (e.g., Tauxe et al., 2008; Tauxe & Kodama, 2009) and also for inclination shallowing correction, we compared the elongation and also the dispersion value directly with the model curve. We consider the results of 10,000 simulations as a "theoretical" estimate of elongation of directions and VGP scatter.

Ten thousand simulations of modified versions of the GGP model TK03.GAD using a modified function from PMAGPY (mktk03) were done to find the GGP model that best describes Mafra and the igneous results from Oslo Graben and Bakaly Formation. The modified function includes changes to the values of g_1^0, α, β, G2, and G3, which are, respectively, the gauss coefficient associated to the mean axial dipolar field, the adjusted parameter proportional to the standard deviations (σ_l), the parameter that differentiates symmetric and antisymmetric components, quadrupolar, and octopolar zonal contributions [see the original values on Table 1 from Tauxe & Kent, 2004]. The first set of simulations were done with the sign of the original g_1^0 changed (original $g_1^0 = -18$ μT, simulated $g_1^0 = +18$ μT) for simulating the reversed field. There is no difference between the elongations and dispersion of VGPs from the original TK03.GAD and the reversed version, so we continue to call it TK03.GAD in Figure 10 (dashed black curves). To illustrate the differences between the Mafra data set and the TK03.GAD model, Figure 10b shows 200 directions predicted by TK03.GAD for the same expected inclination (inc = 69.3°). Figures 10c–10e show directions from modified versions of TK03 model for the same expected inclination.

According to paleosecular variation studies for superchrons (Biggin et al., 2008; de Oliveira et al., 2018; Doubrovine et al., 2019; McFadden et al., 1991), a larger dispersion variation with latitude is expected for superchrons, and an increase in the β parameter is reasonable. Therefore, instead of 3.8 from TK03, we used an arbitrarily higher higher $\beta = 5.0$. Next, we searched for a model that produced a dispersion curve more compatible with the three available results in a sequence of 40 values of α from 0.4 to 15.0. The model with the least absolute differences (total misfit of 4°) in dispersion results had $\alpha = 4.5$ μT for $\beta = 5.0$. This model (continuous black line, Figures 10f and 10g) produces dispersion values close to the results. The elongation of this model is increased for low paleolatitudes. To this model ($\beta = 5.0$, $\alpha = 4.5$ μT), we also added different zonal nondipolar contributions (nonnull G2 and G3). The octopolar component (G3 = 10%) increases the elongation for both hemispheres (dotted green line model, Figures 10f and 10g), and the quadrupolar produces an asymmetric result. The contribution of G2 = −10% produces high elongation for the southern hemisphere and low elongation for the Northern Hemisphere (light-purple dash-dot line model, Figures 10f and 10g).

The sum of absolute differences between the results of elongation and the tested models' curves (Figure 10f) is not so different when we compared the data with TK03 or the other versions of GGP that we ran (GAD, $\alpha = 4.5$ μT and $\beta = 5.0$; 10% of G3; −10% G2). The sum of absolute difference in elongation is reduced from 2.0 for TK03 model to 1.9 for our model (GAD, $\alpha = 4.5$ μT and $\beta = 5.0$). The smallest difference found was for the GGP version with quadrupolar contribution (1.6 of total absolute difference), because the elongation results are not symmetric and plot nearer to this GGP version. The two data sets from the Northern Hemisphere (Bakaly Formation and Oslo Graben), opposite to the Mafra results, have lower elongation than predicted by the model. However, because of the high error bars associated with the elongation results, and similar misfit for every tested model, we are not able to define the shape of the expected distribution of Kiaman times using only the available elongation results.

Although the elongation results did not help to define the shape of distribution, the dispersion results, even for different types of rocks, consistently do not permit the assumption that the TK03 model is valid for Kiaman times. In addition, if we consider for this time our best fitting GGP model (GAD, $\alpha = 4.5$ μT and $\beta = 5.0$) for the dispersion, the predicted elongation curve (black continuous curve) will be also different from TK03. This would imply that the inclination shallowing corrections for sedimentary rocks of this age, assuming the TK03 as valid was improper, especially for low paleolatitudes where the elongation is higher.

It should be noted that perhaps the TK03 model is no longer compatible with the last few million years data because it was fitted to the database available at the end of 1990s. Since then, no new GGP model has been built, but the paleomagnetic database for the recent field has been improved and modified, as we can see in the last compilation made by Cromwell et al. (2018).

These different versions of GGP models were built here only with the intention of speculating what kind of geomagnetic field behavior might represent the available data, so we should also consider that the three data sets have limited number of sites and are from three distinct types of rocks. This limited data set means that any comparisons with the model may be affected by local effects rather than being completely representative of the specific latitude band.

9. Conclusions

The paleomagnetic results of the Mafra Formation presented in this study are the largest known section of primary sedimentary data from Kiaman times with AARM inclination shallowing correction. We presented cyclostratigraphic analyses that permitted inference of the time span for the deposition of the Mafra sampling section. The new paleomagnetic pole of reference for South America is compatible with what is expected for the South American plate for this time; furthermore, all remanent magnetizations are reversed and consistent with what we expect from a primary remanence acquired during a reversed superchron. Also, these sediments are completely flat lying, and despite the lack of folding tests, we know that they were definitely not remagnetized by tectonic effects.

This long primary data set together with other two igneous sections is totally incompatible with the VGP scatter predicted by the TK03 GGP model. Because of the way GGP models are built, the dispersion and elongation predictions cannot be dissociated. If we change the parameters of a GGP model, both parameters will alter. In this study, the reduced dispersion produces an increase in elongations mainly near equatorial latitudes.

Recent paleomagnetic studies of the Upper Paleozoic Era adopted the use of the E/I method for correction of sedimentary data (e.g., Brandt et al., 2009; Franco, Ernesto, et al., 2012; Haldan et al., 2009; Lanci et al., 2013). However, no conclusive test had previously been done attesting the validity of TK03.GAD elongation for the Paleozoic Era. This new result is an alert that the indiscriminate use of E/I method may be dangerous for any period over which the method has not been tested.

Acknowledgments
Comments from two anonymous reviewers improved the paper. This study was supported by the Brazilian funding agency CNPq (308475/2015-1) and in part by the Coordenação de Aperfeiçoamento de Pessoal de Nível Superior-Brasil (CAPES)-Finance Code 88881.186997/2018-01. The data can be found at https://earthref.org/ERDA/2391/ (demagnetization data), https://earthref.org/ERDA/2392/ (rock magnetism data), and in the Tables S1, S2, S3, S4, S5, and S6 of supporting information.

References

Bazhenov, M. L., Van der Voo, R., Menzo, Z., Dominguez, A. R., Meert, J. G., & Levashova, N. M. (2016). Paleomagnetism and dating of a thick lava pile in the Permian Bakaly Formation of eastern Kazakhstan: Regularities and singularities of the paleomagnetic record in thick lava series. *Physics of the Earth and Planetary Interiors*, *253*, 5–20. https://doi.org/10.1016/j.pepi.2016.02.001

Berger, A., & Loutre, M. F. (1994). Astronomical forcing through geologic time. In: De Boer, P.L., Smith, D.G. (Eds.), Orbital forcing and cyclic sequences. *Special Publication of the International Association of Sedimentologists*, *19*, 15–24. https://doi.org/10.1002/9781444304039.ch2

Biggin, A. J., van Hinsbergen, D. J. J., Langereis, C. G., Straathof, G. B., & Deenen, M. H. L. (2008). Geomagnetic secular variation in the Cretaceous normal superchron and in the Jurassic. *Physics of the Earth and Planetary Interiors*, *169*(1-4), 3–19. https://doi.org/10.1016/j.pepi.2008.07.004

Bilardello, D., & M. Jackson (2013). What do the Mumpsies do?, IRM Quarterly, Vol. 23, No. 3.

Brandt, D., Ernesto, M., Rocha-Campos, A. C., & dos Santos, P. R. (2009). Paleomagnetism of the Santa Fe Group, central Brazil: Implications for the late Paleozoic apparent polar wander path for South America. *Journal of Geophysical Research*, *114*, B02101. https://doi.org/10.1029/2008JB005735

Cagliari, J., Philipp, R. P., Buso, V. V., Netto, R. G., Hillebrand, P. K., Lopes, R. C., et al. (2016). Age constraints of the glaciation in the Paraná Basin: Evidence from new U-Pb dates. *Journal of the Geological Society*, *173*(6), 871–874. https://doi.org/10.1144/jgs2015-161

Chadima, M., and F. Hrouda (2006), Remasoft 3.0: A user-friendly paleomagnetic data browser and analyzer, Travaux Géophysiques, 27, 20-21.

Chadima, M., & Jelínek, V. (2008). Anisoft 4.2.—Anisotropy data browser. *Contributions to Geophysics and Geodesy*, *38*(Special Issue), 38–41.

Constable, C. G., & Johnson, C. L. (1999). Anisotropic paleosecular variation models: Implications for geomagnetic field observables. *Physics of the Earth and Planetary Interiors*, *115*(1), 35–51. https://doi.org/10.1016/s0031-9201(99)00065-5

Constable, C. G., & Parker, R. L. (1988). Statistics of the geomagnetic secular variation for the past 5-My. *Journal of Geophysical Research*, *93*(B10), 11,569–11,581. https://doi.org/10.1029/JB093iB10p11569

Cromwell, G., Johnson, C. L., Tauxe, L., Constable, C. G., & Jarboe, N. A. (2018). PSV10: A global data set for 0–10 Ma time-averaged field and paleosecular variation studies. *Geochemistry, Geophysics, Geosystems*, *19*, 1533–1558. https://doi.org/10.1002/2017GC007318

de Oliveira, W. P., Franco, D. R., Brandt, D., Ernesto, M., Neto, C. F. D., Zhao, X. X., et al. (2018). Behavior of the paleosecular variation during the Permian-Carboniferous reversed superchron and comparisons to the low reversal frequency intervals since Precambrian times. *Geochemistry, Geophysics, Geosystems*, *19*, 1035–1048. https://doi.org/10.1002/2017GC007262

Domeier, M., Van der Voo, R., Tohver, E., Tomezzoli, R. N., Vizan, H., Torsvik, T. H., & Kirshner, J. (2011). New Late Permian paleomagnetic data from Argentina: Refinement of the apparent polar wander path of Gondwana. *Geochemistry, Geophysics, Geosystems*, *12*, Q07002. https://doi.org/10.1029/2011GC003616

Domeier, M., Van der Voo, R., Tomezzoli, R. N., Tohver, E., Hendriks, B. W. H., Torsvik, T. H., et al. (2011). Support for an "A-type" Pangea reconstruction from high-fidelity Late Permian and Early to Middle Triassic paleomagnetic data from Argentina. *Journal of Geophysical Research*, *116*, B12114. https://doi.org/10.1029/2011JB008495

Domeier, M., Van der Voo, R., & Torsvik, T. H. (2012). Paleomagnetism and Pangea: The road to reconciliation. *Tectonophysics*, *514-517*, 14–43. https://doi.org/10.1016/j.tecto.2011.10.021

Doubrovine, P. V., Veikkolainen, T., Pesonen, L. J., Piispa, E., Ots, S., Smirnov, A. V., et al. (2019). Latitude dependence of geomagnetic paleosecular variation and its relation to the frequency of magnetic reversals: Observations from the Cretaceous and Jurassic. *Geochemistry, Geophysics, Geosystems*, *20*, 1240–1279. https://doi.org/10.1029/2018GC007863

Dunlop, D., & Ozdemir, O. (1997). *Rock magnetism*, 573 . New York: Cambridge University Press.edited

Ellwood, B. B., Crick, R. E., El Hassani, A., Benoist, S. L., & Young, R. H. (2000). Magnetosusceptibility event and cyclostratigraphy method applied to marine rocks: Detrital input versus carbonate productivity. *Geology*, *28*(12), 1135–1138. https://doi.org/10.1130/0091-7613(2000)28<1135:meacma>2.0.co;2

Ellwood, B. B., Lambert, L. L., Tomkin, J. H., Bell, G. L., Nestell, M. K., Nestell, G. P., & Wardlaw, B. R. (2012). Magnetostratigraphy susceptibility for the Guadalupian series GSSPs (Middle Permian) in Guadalupe Mountains National Park and adjacent areas in West Texas. *Geological Society, London, Special Publications*, *373*(1), 375–394. https://doi.org/10.1144/SP373.1

Ernesto, M. (2005). Paleomagnetism of the post-Paleozoic alkalinemagmatism in the Brazilian Platform: Questioning the mantleplume model. In P. Comin-Chiaramonti, & C. B. Gomes (Eds.), *Mesozoic to Cenozoic alkaline magmatism in the Brazilian Platform*, (pp. 689–705). São Paulo: Edusp/Fapesp.

Ernesto, M., Comin-Chiaramonti, P., & Gomes, C. D. (2015). The Early Triassic magmatism of the Alto Paraguay Province, Central South America: Paleomagnetic and ASM data. *Open Geosciences*, *7*(1), 386–394. https://doi.org/10.1515/geo-2015-0022

Fang, Q., Wu, H. C., Hinnov, L. A., Jing, X. C., Wang, X. L., Yang, T. S., et al. (2017). Astronomical cycles of Middle Permian Maokou Formation in South China and their implications for sequence stratigraphy and paleoclimate. *Palaeogeography, Palaeoclimatology, Palaeoecology*, *474*, 130–139. https://doi.org/10.1016/j.palaeo.2016.07.037

Fisher, R. (1953). Dispersion on a sphere. *Proceedings of the Royal Society of London Series a-Mathematical and Physical Sciences*, *217*(1130), 295–305. https://doi.org/10.1098/rspa.1953.0064

Font, E., Ernesto, M., Silva, P. F., Correia, P. B., & Nascimento, M. A. L. (2009). Palaeomagnetism, rock magnetism and AMS of the Cabo Magmatic Province, NE Brazil, and the opening of South Atlantic. *Geophysical Journal International*, *179*(2), 905–922. https://doi.org/10.1111/j.1365-246X.2009.04333.x

Franco, D. R., Ernesto, M., Ponte-Neto, C. F., Hinnov, L. A., Berquo, T. S., Fabris, J. D., & Rosiere, C. A. (2012). Magnetostratigraphy and mid-palaeolatitude dispersion of VGPs during the Permo-Carboniferous superchron: Results from Parana Basin (Southern Brazil) rhythmites. *Geophysical Journal International*, *191*(3), 993–1014. https://doi.org/10.1111/j.1365-246X.2012.05670.x

Franco, D. R., Hinnov, L. A., & Ernesto, M. (2012). Millennial-scale climate cycles in Permian-Carboniferous rhythmites: Permanent feature throughout geologic time? *Geology*, *40*(1), 19–22. https://doi.org/10.1130/g32338.1

Geuna, S. E., Escosteguy, L., & Limarino, C. Ó. (2010). Paleomagnetism of the Carboniferous-Permian Patquía Formation, Paganzo basin, Argentina: Implications for the apparent polar wander path for South America and Gondwana during the Late Palaeozoic. *Geologica Acta*, *8*(4), 373–397. https://doi.org/10.1344/105.000001578

Geuna, S. E., & Escosteguy, L. D. (2004). Palaeomagnetism of the Upper Carboniferous-Lower Permian transition from Paganzo basin, Argentina. *Geophysical Journal International*, *157*(3), 1071–1089. https://doi.org/10.1111/j.1365-246X.2004.02229.x

Gilder, S., Rousse, S., Farber, D., McNulty, B., Sempere, T., Torres, V., & Palacios, O. (2003). Post-Middle Oligocene origin of paleomagnetic rotations in Upper Permian to Lower Jurassic rocks from northern and southern Peru. *Earth and Planetary Science Letters*, *210*(1–2), 233–248. https://doi.org/10.1016/S0012-821X(03)00102-X

Haldan, M. M., Langereis, C. G., Biggin, A. J., Dekkers, M. J., & Evans, M. E. (2009). A comparison of detailed equatorial red bed records of secular variation during the Permo-Carboniferous Reversed Superchron. *Geophysical Journal International*, *177*(3), 834–848. https://doi.org/10.1111/j.1365-246X.2009.04124.x

Haldan, M. M., Meijers, M. J. M., Langereis, C. G., Larsen, B. T., & Heyer, H. (2014). New palaeomagnetic results from the Oslo Graben, a Permian Superchron lava province. *Geophysical Journal International*, *199*(3), 1554–1571. https://doi.org/10.1093/gji/ggu351

Halls, H. C. (1976). Least-squares method to find a remanence direction from converging remagnetization circles. *Geophysical Journal of the Royal Astronomical Society*, *45*(2), 297–304. https://doi.org/10.1111/j.1365-246X.1976.tb00327.x

Holz, M., Souza, P. A., & Iannuzzi, R. (2008). Sequence stratigraphy and biostratigraphy of the Late Carboniferous to Early Permian glacial succession (Itarare subgroup) at the eastern-southeastern margin of the Parana Basin, Brazil. *Resolving the Late Paleozoic Ice Age in Time and Space*, *441*, 115–129. https://doi.org/10.1130/2008.2441(08)

Hu, P. X., Zhao, X., Roberts, A. P., Heslop, D., & Rossel, R. A. V. (2018). Magnetic domain state diagnosis in soils, loess, and marine sediments from multiple first-order reversal curve-type diagramstaxonomynumbers. *Journal of Geophysical Research: Solid Earth*, *123*, 998–1017. https://doi.org/10.1002/2017JB015195

Irving, E. (1977). Drift of major continental blocks since Devonian. *Nature*, *270*(5635), 304–309. https://doi.org/10.1038/270304a0

Jackson, M. J., Banerjee, S. K., Marvin, J. A., Lu, R., & Gruber, W. (1991). Detrital remanence, inclination errors, and anhysteretic remanence anisotropy—Quantitative model and experimental results. *Geophysical Journal International*, *104*(1), 95–103. https://doi.org/10.1111/j.1365-246X.1991.tb02496.x

Jesinkey, C., Forsythe, R. D., Mpodozis, C., & Davidson, J. (1987). Concordant late Paleozoic paleomagnetizations from the Atacama Desert: Implications for tectonic models of the Chilean Andes. *Earth and Planetary Science Letters*, *85*(4), 461–472. https://doi.org/10.1016/0012-821X(87)90141-5

Johnson, C. L., Constable, C. G., Tauxe, L., Barendregt, R., Brown, L. L., Coe, R. S., et al. (2008). Recent investigations of the 0–5 Ma geomagnetic field recorded by lava flows. *Geochemistry, Geophysics, Geosystems*, *9*, Q04032. https://doi.org/10.1029/2007GC001696

King, R. (1955). The remanent magnetism of artificially deposited sediments. *Geophysical Supplements to the Monthly Notices of the Royal Astronomical Society*, *7*(3), 115–134. https://doi.org/10.1111/j.1365-246X.1955.tb06558.x

Kirschvink, J. L. (1980). The least-squares line and plane and the analysis of paleomagnetic data. *Geophysical Journal of the Royal Astronomical Society*, *62*(3), 699–718. https://doi.org/10.1111/j.1365-246X.1980.tb02601.x

Kodama, K. P. (2009). Simplification of the anisotropy-based inclination correction technique for magnetite- and haematite-bearing rocks: A case study for the Carboniferous Glenshaw and Mauch Chunk Formations, North America. *Geophysical Journal International*, *176*(2), 467–477. https://doi.org/10.1111/j.1365-246X.2008.04013.x

Kodama, K. P. (2012). *Paleomagnetism of sedimentary rocks: Process and interpretation*. Hoboken, NJ: John Wiley & Sons. https://doi.org/10.1002/9781118384138

Kodama, K. P., Anastasio, D. J., Newton, M. L., Pares, J. M., & Hinnov, L. A. (2010). High-resolution rock magnetic cyclostratigraphy in an Eocene flysch, Spanish Pyrenees. *Geochemistry, Geophysics, Geosystems*, *11*, Q0AA07. https://doi.org/10.1029/2010GC003069

Koester, E., A. K. Scomazzon, L. C. Weinschütz, E. Wilner, L. P. Moutinho, and S. Nascimento (2016), Idade Rb-Sr do folhelho Lontras, Grupo Itararé, Bacia do Paraná, na região de Mafra, SC, Brasil, in Anais do 48o Congresso Brasileiro de Geologia "As geotecnologias e o século XXI" edited, Porto Alegre - Brasil.

Lanci, L., Muttoni, G., & Erba, E. (2010). Astronomical tuning of the Cenomanian Scaglia Bianca Formation at Furlo, Italy. *Earth and Planetary Science Letters*, *292*(1-2), 231–237. https://doi.org/10.1016/j.epsl.2010.01.041

Lanci, L., Tohver, E., Wilson, A., & Flint, S. (2013). Upper Permian magnetic stratigraphy of the lower Beaufort group, Karoo basin. *Earth and Planetary Science Letters*, *375*, 123–134. https://doi.org/10.1016/j.epsl.2013.05.0172013.05.017

Latta, D. K., Anastasio, D. J., Hinnov, L. A., Elrick, M., & Kodama, K. P. (2006). Magnetic record of Milankovitch rhythms in lithologically noncyclic marine carbonates. *Geology*, *34*(1), 29–32. https://doi.org/10.1130/g21918.1

McElhinny, M. W., & McFadden, P. L. (1997). Palaeosecular variation over the past 5 Myr based on a new generalized database. *Geophysical Journal International*, *131*(2), 240–252. https://doi.org/10.1111/j.1365-246X.1997.tb01219.x

McFadden, P. L., & McElhinny, M. W. (1988). The combined analysis of remagnetization circles and direct observations in paleomagnetism. *Earth and Planetary Science Letters*, *87*(1-2), 161–172. https://doi.org/10.1016/0012-821x(88)90072-6

McFadden, P. L., Merrill, R. T., McElhinny, M. W., & Lee, S. H. (1991). Reversals of the earths magnetic-field and temporal variations of the dynamo families, *journal of. Geophysical Research-Solid Earth and Planets*, *96*(B3), 3923–3933. https://doi.org/10.1029/90jb02275

Milani, E. J. (1997). *Evolução tectono-estratigráfica da Bacia do Paraná e seu relacionamentocom a geodinâmica fanerozóica do Gondwana sul-oriental*. Rio Grande do Sul, Brazil: Universidade Federal do Rio Grande do Sul.

Mudelsee, M. (2014). *Climate time series analysis: Classical statistical and bootstrap methods*, (2nd ed.). Dordrecht: Springer. 454 pp

Opdyke, M. D., & Channell, J. E. (1996). *Magnetic stratigraphy*. San Diego, CA: Academic Press.

Opdyke, N. D., & Henry, K. W. (1969). A test of the dipole hypothesis. *Earth and Planetary Science Letters*, *6*(2), 139–151. https://doi.org/10.1016/0012-821x(69)90132-0

Quidelleur, X., & Courtillot, V. (1996). On low-degree spherical harmonic models of paleosecular variation. *Physics of the Earth and Planetary Interiors*, *95*(1-2), 55–77. https://doi.org/10.1016/0031-9201(95)03115-4

Rakotosolofo, N. A., Tait, J. A., Carlotto, V., & Cárdenas, J. (2006). Palaeomagnetic results from the Early Permian Copacabana Group, southern Peru: Implication for Pangaea palaeogeography. *Tectonophysics*, *413*(3–4), 287–299. https://doi.org/10.1016/j.tecto.2005.10.043

Rapalini, A. E., Fazzito, S., & Orué, D. (2006). A new Late Permian paleomagnetic pole for stable South America: The Independencia group, eastern Paraguay. *Earth, Planets and Space*, *58*(10), 1247–1253. https://doi.org/10.1186/BF03352620

Rapalini, A. E., & Vilas, J. F. (1991). Tectonic rotations in the Late Palaeozoic continental margin of southern South America determined and dated by palaeomagnetism. *Geophysical Journal International*, *107*(2), 333–351. https://doi.org/10.1111/j.1365-246X.1991.tb00829.x

Scheidegger, A. (1965), On the statistics of the orientation of bedding planes, grain axes, and similar sedimentological data, US Geological Survey Professional Paper, 525, 164-167.

Schneider, R. L., Mühlmann, H., Tommasi, E., Medeiros, R. A. A., Daemon, R. F., & Nogueira, A. A. (1974). Revisão estratigráfica da bacia do Paraná. In *Anais do 28 Congresso Brasileiro de Geologia* (pp. 41–65). Porto Alegre, Brazil: Sociedade Brasileira de Geologia (SBG).

Strauss, B. E., Strehlau, J. H., Lascu, I., Dorale, J. A., Penn, R. L., & Feinberg, J. M. (2013). The origin of magnetic remanence in stalagmites: Observations from electron microscopy and rock magnetism. *Geochemistry, Geophysics, Geosystems*, *14*, 5006–5025. https://doi.org/10.1002/2013GC004950

Strehlau, J. H., Hegner, L. A., Strauss, B. E., Feinberg, J. M., & Penn, R. L. (2014). Simple and efficient separation of magnetic minerals from speleothems and other carbonates. *Journal of Sedimentary Research*, *84*(11), 1096–1106. https://doi.org/10.2110/jsr.2014.89

Tauxe, L., Banerjee, S., Butler, R., & Van der Voo, R. (2016). *Essentials of paleomagnetism*, (4th Web ed., edited). California: California University Press.

Tauxe, L., & Kent, D. V. (2004). A simplified statistical model for the geomagnetic field and the detection of shallow bias in paleomagnetic inclinations: Was the ancient magnetic field dipolar? *Timescales of the Paleomagnetic Field*, *145*, 101–115. https://doi.org/10.1029/145gm08

Tauxe, L., & Kodama, K. P. (2009). Paleosecular variation models for ancient times: Clues from Keweenawan lava flows. *Physics of the Earth and Planetary Interiors*, *177*(1-2), 31–45. https://doi.org/10.1016/j.pepi.2009.07.006

Tauxe, L., Kodama, K. P., & Kent, D. V. (2008). Testing corrections for paleomagnetic inclination error in sedimentary rocks: A comparative approach. *Physics of the Earth and Planetary Interiors*, *169*(1-4), 152–165. https://doi.org/10.1016/j.pepi.2008.05.006

Tauxe, L., Shaar, R., Jonestrask, L., Swanson-Hysell, N. L., Minnett, R., Koppers, A. A. P., et al. (2016). PmagPy: Software package for paleomagnetic data analysis and a bridge to the Magnetics Information Consortium (MagIC) Database. *Geochemistry, Geophysics, Geosystems*, *17*, 2450–2463. https://doi.org/10.1002/2016GC006307

Thomson, D. J. (1982). Spectrum estimation and harmonic analysis. *Proceedings of the IEEE*, *70*(9), 1055–1096. https://doi.org/10.1109/PROC.1982.12433

Torsvik, T. H., van der Voo, R., Preeden, U., Mac Niocaill, C., Steinberger, B., Doubrovine, P. V., et al. (2012). Phanerozoic polar wander, palaeogeography and dynamics. *Earth-Science Reviews*, *114*(3-4), 325–368. https://doi.org/10.1016/j.earscirev.2012.06.007

Vandamme, D. (1994). A new method to determine paleosecular variation. *Physics of the Earth and Planetary Interiors*, *85*(1-2), 131–142. https://doi.org/10.1016/0031-9201(94)90012-4

Weinschütz, L. C., & Castro, J. C. D. (2004). Arcabouço cronoestratigráfico da Formação Mafra (intervalo médio) na região de Rio Negro/PR - Mafra/SC, borda leste da bacia do Paraná. *Rem: Revista Escola de Minas*, *57*, 151–156. https://doi.org/10.1590/S0370-44672004000300003

Wu, H. C., Zhang, S. H., Feng, Q. L., Jiang, G. G., Li, H. Y., & Yang, T. S. (2012). Milankovitch and sub-Milankovitch cycles of the early Triassic Daye Formation, South China and their geochronological and paleoclimatic implications. *Gondwana Research*, *22*(2), 748–759. https://doi.org/10.1016/j.gr.2011.12.003

Yokoyama, E., Brandt, D., Tohver, E., & Trindade, R. I. F. (2014). Palaeomagnetism of the Permo-Triassic Araguainha impact structure (Central Brazil) and implications for Pangean reconstructions. *Geophysical Journal International*, *198*(1), 154–163. https://doi.org/10.1093/gji/ggu125

Zhao, X., Heslop, D., & Roberts, A. P. (2015). A protocol for variable-resolution first-order reversal curve measurements. *Geochemistry, Geophysics, Geosystems*, *16*, 1364–1377. https://doi.org/10.1002/2014GC005680

Zhao, X., Roberts, A. P., Heslop, D., Paterson, G. A., Li, Y. L., & Li, J. H. (2017). Magnetic domain state diagnosis using hysteresis reversal curves. *Journal of Geophysical Research: Solid Earth*, *122*, 4767–4789. https://doi.org/10.1002/2016JB013683